



**HAL**  
open science

## Morphodynamic modelling of beach cusp formation: The role of wave forcing and sediment composition

Christopher Daly, France Floc'H, Luis P.M. Almeida, Rafael Almar, Marion  
Jaud

► **To cite this version:**

Christopher Daly, France Floc'H, Luis P.M. Almeida, Rafael Almar, Marion Jaud. Morphodynamic modelling of beach cusp formation: The role of wave forcing and sediment composition. *Geomorphology*, 2021, 389, pp.107798. 10.1016/j.geomorph.2021.107798 . hal-03342411

**HAL Id: hal-03342411**

**<https://hal.univ-brest.fr/hal-03342411>**

Submitted on 13 Jun 2023

**HAL** is a multi-disciplinary open access archive for the deposit and dissemination of scientific research documents, whether they are published or not. The documents may come from teaching and research institutions in France or abroad, or from public or private research centers.

L'archive ouverte pluridisciplinaire **HAL**, est destinée au dépôt et à la diffusion de documents scientifiques de niveau recherche, publiés ou non, émanant des établissements d'enseignement et de recherche français ou étrangers, des laboratoires publics ou privés.



Distributed under a Creative Commons Attribution - NonCommercial 4.0 International License

# Morphodynamic modelling of beach cusp formation: the role of wave forcing and sediment composition

Christopher J. Daly<sup>a,b,\*</sup>, France Floc'h<sup>b</sup>, Luis P.M. Almeida<sup>c</sup>, Rafael Almar<sup>a</sup>, Marion Jaud<sup>b</sup>

<sup>a</sup>*LEGOS, IRD, 31400 Toulouse, France*

<sup>b</sup>*University of Brest, CNRS, IUEM, UMR 6538 Géosciences Océan, 29290 Plouzané, France*

<sup>c</sup>*Universidade Federal do Rio Grande, Rio Grande do Sul, Brazil*

---

## Abstract

A field of beach cusps formed during a field experiment at Nha Trang Beach, Vietnam, under accretive conditions. The measured data was used to set-up morphodynamic simulations in XBeach, which was able to simulate cusp formation from an initially long-shore uniform beach profile. Several types of simulations were run in order to observe the resulting variation in mean cusp dimensions (length, depth and height), swash flow patterns, and sediment sorting. Both time-constant (JONSWAP) and time-varying (measured) wave forcing conditions were superimposed on the measured tide. In the former, four wave parameters were varied (wave height, period, direction, and spreading), while in the latter, the median sediment size and sediment composition were varied. The wave period was found to primarily influence long-shore length scales, the wave height cross-shore length scales, and obliquely incident waves enhance all these dimensions particularly under narrow-banded conditions. Cusps are not prominent if the wave energy is too low to effect

---

\*Corresponding Author: [dalyjchris@gmail.com](mailto:dalyjchris@gmail.com)

significant onshore transport, if the wave angle of incidence and spreading are too large (effectively smoothing out swash perturbations), or if the sediment is too fine in relation to the wave conditions (dissipative beaches or highly erosive wave conditions). Coarse sediment generally tends to be located on cusp horns above the waterline, but is otherwise variable depending on cross-shore location and tide levels. As the XBeach model results show large agreement with well-established norms, it may therefore be used to more rigorously study processes that help to initiate cusps in future work.

*Keywords:* Beach cusps, Onshore sediment transport, Pattern formation, Wave forcing, Sediment sorting

---

## 1 **1. Introduction**

2 Rhythmic cusped features are commonly observed on sandy beaches with  
3 wavelengths up to  $\sim 1$  km. Of these, those with long-shore wavelengths (spac-  
4 ing) up to  $\sim 50$  m are usually considered to be formed under swash-dominant  
5 processes. Numerous field studies have repeatedly shown that beach cusps  
6 generally form during calm, narrow-banded, shore-normal wave conditions  
7 which promote accretion (Holland, 1998; Almar et al., 2008; Vourdoukas,  
8 2012; O’Dea and Brodie, 2019). Cusps also form (less frequently) under en-  
9 ergetic or erosive conditions, and their morphological development is often  
10 dynamic, featuring long-shore migration in which new cusp fields are gen-  
11 erated over pre-existing formations (Masselink et al., 1997; Masselink and  
12 Pattiaratchi, 1998b; van Gaalen et al., 2011). The presence of cusps depends  
13 on local characteristics such as sediment size, beach slope and wave energy  
14 (van Gaalen et al., 2011), with cusps being more prevalent on steep, coarse

15 grained, reflective beaches. Cusps are frequently characterised by their spac-  
16 ing, which is thought to be determined by the wavelength of edge waves  
17 (Guza and Inman, 1975) or a function of the swash excursion (Coco et al.,  
18 2001; Sunamura, 2004).

19 Cusps are often thought to develop via two primary mechanisms: 1) wave  
20 height patterns caused by edge waves in the long-shore dimension (Inman and  
21 Guza, 1982), or 2) from self-organisation which allows small bathymetric per-  
22 turbations to grow through positive morphodynamic feedback mechanisms  
23 (Werner and Fink, 1993; Coco et al., 1999). Whether or not edge waves,  
24 self organisation, or a combination of both theories are responsible for beach  
25 cusp formation remains an open question (Holland and Holman, 1996; O’Dea  
26 and Brodie, 2019). Recent numerical simulations of nearshore flow patterns  
27 suggest that wave reflection over steep beaches can also be a mechanism for  
28 beach cusp formation (Almar et al., 2018). While much research, based on  
29 these pioneering works, has been focused on the question of how cusps are ini-  
30 tiated, it is also important to understand how they evolve once formed under  
31 varying wave conditions and beach types (Holland, 1998; van Gaalen et al.,  
32 2011). Furthermore, while most of what is known about cusp development  
33 is based on field observations, numerical simulations have provided valuable  
34 insight into how cusps are formed (Werner and Fink, 1993; Coco et al., 2000),  
35 what processes are important for their development (Dodd et al., 2008), how  
36 their geometry affects swash flow patterns (Masselink et al., 1997), and how  
37 surf zone circulation affects cusp development (Garnier et al., 2010). Nu-  
38 merical simulations may therefore be used to glean knowledge on how cusps  
39 respond to changes in wave forcing and sediment composition, and to predict

40 cusp morphology for specific locations.

41 Numerical simulations of cusp development often require specialized mod-  
42 els capable of resolving swash dynamics and processes such as short wave  
43 runup, swash sediment transport, and groundwater infiltration and exfiltra-  
44 tion (Coco et al., 2000, 2003; Dodd et al., 2008). It is also important to  
45 consider other processes such as sediment exchange between the swash and  
46 surf zone, wave-wave (bore) interactions and turbulence, and infragravity  
47 wave runup (Bakhtyar et al., 2009). Coco et al. (2000) and Dodd et al.  
48 (2008) used a cellular automata and process-based modelling approach, re-  
49 spectively, to allow cusps to form from an initially long-shore uniform beach  
50 profile, in which sediment was reworked in the swash. As these simulations  
51 were initiated at the base of the swash, surf zone processes were not included.  
52 On the other hand, Garnier et al. (2010) excludes swash zone processes from  
53 their simulations, which showed that inner surf zone processes may enhance  
54 cusp development higher up on the beachface. Using established morpho-  
55 dynamic nearshore models, such as XBeach (Roelvink et al., 2009), one can  
56 simulate the entire range from surf to swash including processes important  
57 in the development of cusps.

58 The Kingsday version of XBeach (Roelvink et al., 2015) includes a wave-  
59 resolving (non-hydrostatic) model, similar to a one-layer implementation of  
60 SWASH (Zijlema et al., 2011), and an underlying surfbeat model which allows  
61 both short and infragravity waves to be resolved in the swash. Several studies  
62 have shown the applicability of the SWASH and XBeach models to simulate  
63 wave runup, infragravity motions, swash hydrodynamics and nearshore cir-  
64 culation (de Bakker et al., 2014; Lashley et al., 2018; Almar et al., 2018;

65 Roelvink et al., 2018). While the coupling of the sediment transport module  
66 with the non-hydrostatic wave solver is still under development, it has been  
67 used experimentally in Daly et al. (2017) and Ruffini et al. (2020). In partic-  
68 ular, Daly et al. (2017) showed that it is possible to simulate beach accretion  
69 and berm formation in XBeach, a key process in the development of cusps.

70 Here, we use the XBeach model to expand the work of Daly et al. (2017)  
71 from a 1D to a 2D domain in order to simulate beach cusp formation and  
72 evolution under varying wave forcing conditions and sediment composition.  
73 The model is benchmarked using data observed during a field campaign at  
74 Nha Trang Beach, Vietnam, in November 2015, during which beach cusps  
75 formed quickly during an accretionary stage lasting for a few days. We aim to  
76 evaluate the performance of the model by comparing predicted length scales,  
77 sediment sorting, and swash circulation patterns to what is expected based on  
78 observations at Nha Trang Beach and that presented in the literature. Based  
79 on the evaluation of the model performance, more detailed investigation into  
80 key processes that influence cusp initiation may be carried out in future work.

## 81 **2. Methods**

### 82 *2.1. Location and Measured Data*

83 An 8-day field experiment was performed at Nha Trang beach, Vietnam,  
84 from 27 November to 4 December 2015 ( $12^{\circ} 15.17'$  N,  $109^{\circ} 11.81'$  E, Fig.  
85 1). A 1200 kHz acoustic Doppler current profiler (ADCP) placed offshore  
86 at 15 m depth measured significant wave heights varying between 0.6 and  
87 1.5 m, and mean wave periods varying between 7 and 12 s (Fig. 2a). Wave  
88 transformation along an instrumented cross-shore transect in the surf and

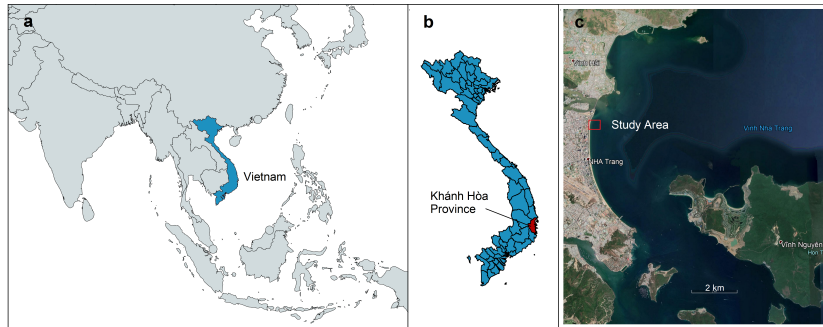


Figure 1: Location of the Nha Trang beach study site (red box in panel c), in the Khánh Hòa Province (red area in panel b), of Vietnam, southeast Asia (blue area in panel a).

89 swash zone were measured using four pressure transducers. A 25 Hz SICK  
 90 LMS511 2D laser scanner was used to measure surface elevation (both of  
 91 the bed and water) in the swash along the same transect, from which the  
 92 swash excursion, swash height and beach slope is determined (Fig. 2b–c).  
 93 The beach is composed of coarse grained sediment (median grain size,  $D_{50}$   
 94 = 0.5 mm) and is located in a diurnal, micro-tidal environment (tide range  
 95 = 1.6 m). As a result, the beach has a fairly steep (1:8) swash slope and a  
 96 narrow low tide terrace. Beach topography data was measured using high-  
 97 resolution drone photogrammetry (output resolution of data points being  
 98 2.85 cm) and closely spaced ( $\sim 10$  m) RTK-GPS transects over a 1 km length  
 99 of beach, centered on the instrumented cross-shore transect. The surveys  
 100 were carried out daily and captured the rapid formation of accretionary beach  
 101 cusps between 28 November and 1 December (Fig. 3). Based on these  
 102 measurements, the cusps had a mean spacing of approximately 28 m. Further  
 103 details of the setup of the field experiment are presented in Almeida et al.  
 104 (2020) and Daly et al. (2017).

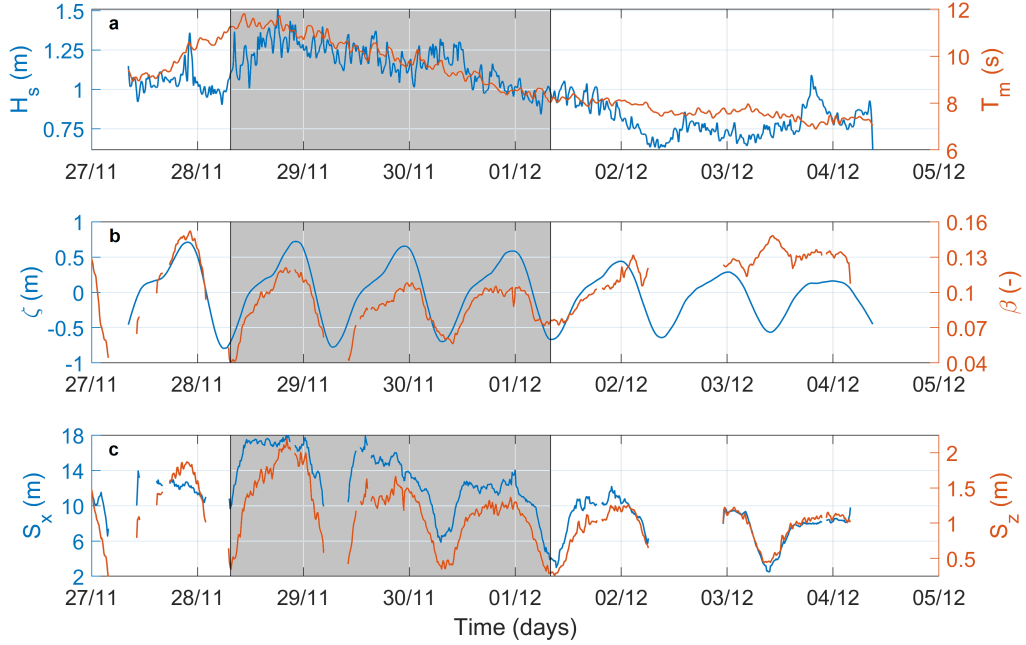


Figure 2: Wave conditions measured at the offshore ADCP and swash geometry measured with LIDAR at Nha Trang during the 2015 field experiment. (Panel a) significant wave height,  $H_s$ , and mean wave period,  $T_m$ . (Panel b) tide elevation,  $\zeta$ , and beach slope,  $\beta$ . (Panel c) swash excursion,  $S_x$ , and swash height,  $S_z$ . The three-day simulation period for Series C is highlighted in grey.

105 *2.2. Numerical Model*

106 *2.2.1. Model Description*

107 The Kingsday version of XBeach (cf. XBeach user manual, (Roelvink  
 108 et al., 2015)) is used here with the non-hydrostatic wave solver (fully wave-  
 109 resolving) enabled, rather than the default surf-beat mode (wave-group-  
 110 resolving). The non-hydrostatic mode gives a better representation of waves  
 111 in the swash zone by combining both short and infragravity parts of the wave  
 112 spectrum, albeit at the expense of having to use a much more highly resolved



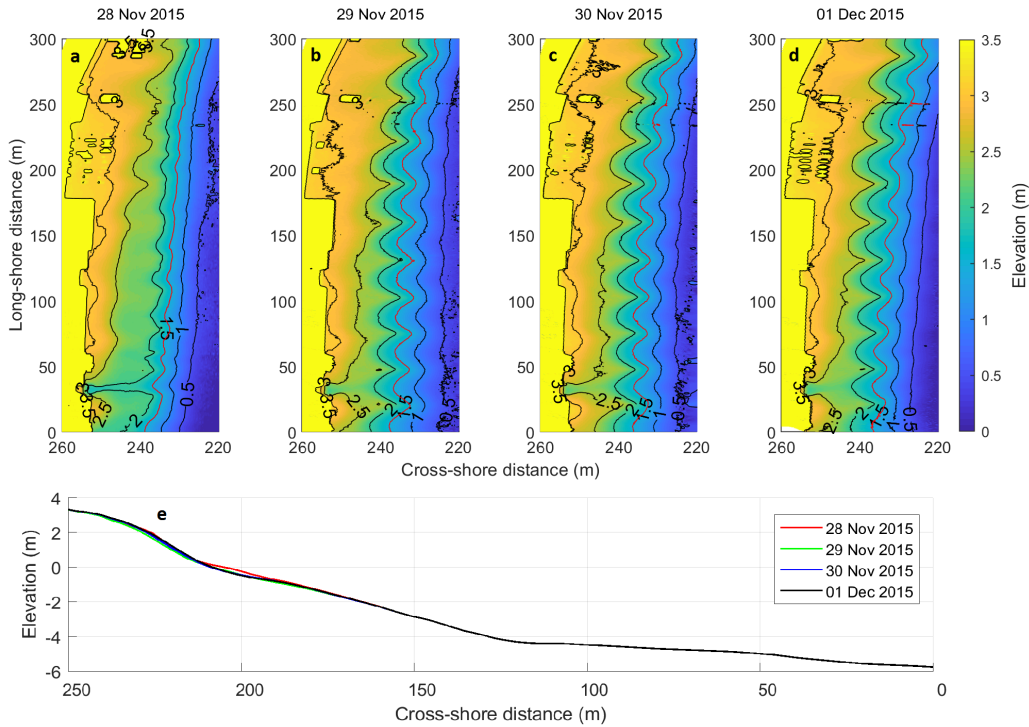


Figure 3: (Panels a-d) Measured elevations at Nha Trang during the field experiment from drone photogrammetry. Changes in morphology show the emergence of beach cusps over 3 days from 28 November (top left) to 1 December (top right), 2015. (Panel e) Long-shore-averaged cross-shore profile of the measured bathymetry.

113 computational grid. In non-hydrostatic mode, short-wave non-linearity is im-  
 114 plicitly accounted for in the flow velocity at the bed, without the need for  
 115 corrections based on estimates of asymmetry and skewness (e.g. Ruessink  
 116 et al. (2012)). Sediment transport is computed based on mean flow con-  
 117 ditions averaged over the wave period using advection-diffusion equations,  
 118 where the Eulerian flow velocity is applied to the bed and suspended load  
 119 transport formulations of Soulsby (1997), van Rijn (2007a) and van Rijn  
 120 (2007b). Mean cross-shore flow (and thus, bed-load transport) tends to be

121 negative (offshore-directed), driven by undertow (van der Werf et al., 2017).  
122 In nature this can be effectively counter-balanced by non-linear wave-induced  
123 accelerations which promote net onshore transport, resulting in accretion  
124 (Elgar et al., 2001). Such intra-wave accelerations are not yet accounted  
125 for in XBeach non-hydrostatic mode as sediment transport calculations are  
126 wave-averaged, resulting in a tendency for the model to over-predict erosion.  
127 However, Daly et al. (2017) produced simulations of Nha Trang which al-  
128 lowed accretion of the beach. This rather unexpected result was found by  
129 using a combination of parameter settings which essentially modified the bed  
130 load transport direction in shallow water such that it is constantly positive  
131 (onshore-directed). Suspended load transport, however, is not affected, and  
132 can be both positive or negative. Therefore, although XBeach may be run  
133 with default parameter settings, some modifications are required for simu-  
134 lating swash morphodynamics, discussed following.

### 135 *2.2.2. Modified Parameter Settings and Prior Validation*

136 Identical parameter settings are used in the current suite of simulations  
137 as presented in Daly et al. (2017), shown in Table 1 below. Four groups of  
138 model parameters are changed from their default setting, relating to 1) bed  
139 friction (*bedfriction* and *bedfriccoef*), 2) bed slope effects (*facsl* and *bdslop-*  
140 *effdir*), 3) hindered erosion (*dilatancy*), and 4) groundwater flow (*gwflow*,  
141 *gw0*, *kx/ky/kz* and *gwhorinfil*). A detailed description of the role each group  
142 of parameters play in achieving onshore transport is given in Daly et al.  
143 (2017), and mentioned briefly here. 1) The Manning bed friction model is  
144 used as it assigns higher friction values to shallow depths than Chézy (de-  
145 fault model), thereby slightly damping flow velocities and allowing increased

146 sediment settling and berm formation in the upper swash. 2) The parame-  
 147 ters controlling bed slope effects modify the direction and magnitude of bed  
 148 load transport based on the bed slope (cf. Walstra et al. (2007)) using the  
 149 model of Talmon et al. (1995). 3) Dilatancy effects hinder erosion under  
 150 high swash flows as under-pressure in the bed reduces water inflow, making  
 151 it more difficult for sediment to become entrained. Dilatancy is accounted for  
 152 by limiting the critical Shields number (cf. van Rhee (2010)). Finally, 4) the  
 153 groundwater flow module allows water infiltration (exfiltration) into (from)  
 154 the bed. Infiltration in the upper swash allows sediment deposits to build  
 155 up and form berms, and is therefore a critical process in simulating swash  
 156 morphodynamics. Groundwater is modelled using Darcy flow equations (cf.  
 157 McCall et al. (2012)), and depends on the permeability of the sediment.

<b>Keyword</b>	<b>Function</b>	<b>Value</b>
<i>bedfriction</i>	Bed friction formulation	Manning
<i>bedfriccoef</i>	Bed friction coefficient	0.02
<i>facsl</i>	Bed slope effect factor	0.15
<i>bdslopeffdir</i>	Modify sediment transport direction	Talmon
<i>dilatancy</i>	Turn on/off dilatancy	1 (on)
<i>gwflow</i>	Turn on/off groundwater flow	1 (on)
<i>gw0</i>	Groundwater level	0.28 m
<i>kx/ky/kz</i>	Darcy flow permeability coefficient	0.001
<i>gwhorinfil</i>	Turn on/off horizontal infiltration	1 (on)

Table 1: XBeach model settings changed from default

158 The modified model settings in Table 1 have been validated for the lo-  
 159 cation at Nha Trang Beach in Daly et al. (2017). Their simulations were  
 160 done over the 1-dimensional long-shore-averaged beach profile starting on 27

161 November 2015 and run for 6 days. Comparisons between the model output  
162 and measured  $H_s$  data at several locations in the inner surf and swash zone  
163 had an average root-mean-square error of 0.15 m and correlation coefficient  
164 of 0.94. Furthermore, comparison between the simulated and measured mean  
165 cross-shore profile showed a root-mean-square error of 0.11 m. Those results  
166 showed that the model reproduces wave transformation up to the swash zone  
167 quite well, and also reasonably predicts berm formation on the upper beach.  
168 Further validation of the model is therefore not necessary here, as the focus  
169 of the study now shifts to assessing the effect varying wave conditions and  
170 sediment composition has on cusp formation.

### 171 *2.3. Numerical Simulations*

#### 172 *2.3.1. Model Grid and Timing*

173 The mean cross-shore profile of the study area on 28 November is used to  
174 create a long-shore uniform initial bathymetry for the model (Fig. 3e). When  
175 using the non-hydrostatic wave mode in XBeach, a detailed computational  
176 grid is required. As such, a grid spacing of 0.75 and 1.5 m in the cross-shore  
177 and long-shore directions are used in the surf and swash zone (area above  
178 2 m depth), respectively. Initial tests with a finer cross-shore grid spacing  
179 of 0.5 m did not significantly change the final result. At the offshore model  
180 boundary, the water depth is 6 m and a maximum cross-shore spacing of 2 m  
181 is used, which gradually decreases toward the resolution used in the surf and  
182 swash zone. The grid spacing used allows waves down to 3 s to be clearly  
183 resolved across the entire domain with a minimum 8 points per wavelength  
184 (and 16 points per wavelength for periods over 7 s). The high resolution grid  
185 in the surf and swash zone also allows beach cusps with wavelengths upwards

186 of 12 m to be adequately resolved.

187 All simulations are run for a period of three days, representing the period  
188 during which cusps formed during the field experiment between 28 November  
189 and 1 December, 2015, (Fig. 3). The three day period is expected to be  
190 sufficient time for cusps to fully form in the model, given that it took only one  
191 day for them to emerge during the field experiment. As the computational  
192 effort for each simulation is expensive, a modest morphological acceleration  
193 factor (*morfac*) of 6 is used to speed up the simulations. Comparable results  
194 were obtained for test simulations run with *morfac* turned on and off. The  
195 model determines the time step based on a prescribed maximum Courant  
196 number (0.7 by default).

197 The output model domain is limited to a dedicated  $240 \times 250$  m area in  
198 the long-shore ( $y$ ) and cross-shore ( $x$ ) dimensions, respectively. This area is  
199 sufficient to observe the development of cusps with long-shore wavelengths up  
200 to 60 m (minimum 4 wavelengths within the domain). A buffer area is added  
201 at either end of the output model domain to account for boundary effects,  
202 especially in cases where waves approach the beach at an oblique angle and  
203 create shadow zones. This area is removed during the post-processing of  
204 the results. In order to limit the size of the output files, time-averaged and  
205 instantaneous global variables (i.e. 2-dimensional) are saved every 10 minutes  
206 (e.g. bed levels, surface elevation, velocity and bed composition). A more  
207 highly resolved time series is saved every 0.5 s for output variables at several  
208 points along the central cross-shore transect (at  $y = 120$  m).

209 *2.3.2. Wave Conditions and Sediment Composition*

210 Simulations are run using either time-constant or time-varying (measured) wave forcing conditions. All simulations are run with the same time-varying (measured) diurnal tidal water levels imposed on the model boundary. For simulations with time-constant wave forcing, a random time-series of surface waves are generated using a JONSWAP spectrum defined by four parameters: the significant wave height ( $H_s$ ), mean wave period ( $T_m$ ), directional spreading ( $\sigma$ ), and angle of incidence ( $\theta$ ). The values of  $H_s$  and  $T_m$  fall within close range of the measured conditions during the field experiment (cf. Fig. 2). A *base case* simulation uses  $[H_s, T_m, \sigma, \theta] = [1.3 \text{ m}, 10 \text{ s}, 0^\circ, 0^\circ]$ . From this simulation, each parameter is varied with values shown in Table 2 below. The 2-dimensional  $H_s$ - $T_m$  parameter space is completely filled with the exception that at  $H_s = 0.7 \text{ m}$  there is no simulation at  $T_m = 11.4 \text{ s}$ , and at  $H_s = 1.7 \text{ m}$  there is no simulation at  $T_m = 7.3 \text{ s}$ , as these wave conditions are far from those observed. The parameter space for  $\sigma$  and  $\theta$  is 1-dimensional. There are 14 time-constant wave simulations for the  $H_s$ - $T_m$  parameter space (Series A1 – A14, including the *base case* at A10), and 6 other simulations for the  $\sigma$  and  $\theta$  parameter space (Series B1 – B6).

Wave Parameter	Values Used
$H_s$ (m)	[ 0.7, 1.0, 1.3, 1.7 ]
$T_m$ (s)	[ 7.3, 8.7, 10.0, 11.4 ]
$\sigma$ ( $^\circ$ )	[ 0, 5, 10, 15 ]
$\theta$ ( $^\circ$ )	[ 0, 5, 10, 15 ]

Table 2: Wave parameter values used to define JONSWAP boundary wave conditions

227 Simulations using time-varying (measured) wave conditions directly use

228 the time-series of wave conditions recorded by the offshore ADCP during the  
 229 field campaign (cf. Fig. 2). The wave direction is, however, kept constant  
 230 at 0 ° (normally incident). The median grain size,  $D_{50}$ , is varied in these  
 231 simulations as [ 0.5, 0.3, 0.2, 0.5/0.2 ] mm (Series C1 – C4, respectively).  
 232 The first (0.5 mm) represents the native size of sediment of the beach while  
 233 the other sizes are exploratory. The latter size (0.5/0.2 mm) features an  
 234 evenly mixed sediment bed of coarse and fine sediment, respectively.

### 235 *2.3.3. Analysis of Results*

236 Contour lines are extracted from output bed level data between -1.5 and  
 237 2.5 m elevation at 0.1 m intervals. The spatial dimensions of the beach cusps  
 238 produced during the simulations are determined by Fourier analysis of each  
 239 contour level at each point in time, yielding the mean long-shore wavelength  
 240 (or cusp spacing,  $L_y$ ) and cross-shore depth ( $L_x$ ). Similarly, the vertical  
 241 height ( $L_z$ ) of the cusps are derived from the analysis of the detrended long-  
 242 shore bed level at each cross-shore location. Variation of the bathymetry ( $z_b$ )  
 243 in the long-shore dimension ( $z_{b,y}$ ) is computed by removing the long-shore  
 244 mean profile ( $\overline{z_{b,y}}$ ) from each cross-shore transect:

$$\widetilde{z_{b,y}} = z_b - \overline{z_{b,y}} \quad (1)$$

245 Here,  $\widetilde{\dots}$  represents long-shore (spatial) fluctuations. Subsequently, the  
 246 root-mean-square (RMS) long-shore bed level variation ( $\Delta$ ), which indicates  
 247 the degree of vertical variability in bed levels and thus prominence of the  
 248 cusps features, is computed as:

$$\Delta = \sqrt{\sum_{z_b=0.5}^{z_b=1.0} \widetilde{z}_{b,y}^2} \quad (2)$$

249 While  $L_z$  more closely indicates the range (maximum - minimum) of the  
 250 vertical height of cusped features,  $\Delta$  values are closer to the mean. Only  
 251 data located between 0.5 and 1.0 m elevation are used Eq. 2 – an area  
 252 in which cusp features are consistently located for most simulations. Final  
 253 values of  $L_y$ ,  $L_x$  and  $L_z$  are extracted as the mean over the 15-minute period  
 254 before and after the time of the last mid-tide at 2.83 days, and further, as the  
 255 mean of values between 0.5 and 1.0 m elevation. Beach cusps are considered  
 256 to be present if final values of  $\Delta > 2$  cm,  $L_z > 5$  cm and the aspect ratio  
 257 ( $AR = L_y/L_x$ )  $< 25$ . They are also considered to be prominent if  $\Delta > 10$   
 258 cm,  $L_z > 20$  cm and  $AR < 10$ .

259 Long-shore variation (or anomaly) of the time-averaged (over a 10 minute  
 260 period) significant wave height and cross-shore current ( $u$ ) field over the  
 261 model domain ( $\langle \widetilde{H}_{s,y} \rangle$  and  $\langle \widetilde{u}_y \rangle$ , respectively) are also computed in a similar  
 262 fashion as  $\widetilde{z}_{b,y}$  in Eq. 1. Here,  $\langle \dots \rangle$  represents the 10-minute time average.  
 263 Turbulent kinetic energy (TKE,  $k$ ) is computed from the time series output  
 264 of cross-shore and long-shore velocity components ( $u$  and  $v$ , respectively)  
 265 along the central cross-shore transect as:

$$k = \frac{1}{2} \left( \langle (u')^2 \rangle + \langle (v')^2 \rangle \right) \quad (3)$$

266 where  $u'$  and  $v'$  are (temporal) fluctuations of the velocity components after  
 267 removal of the mean over a sample period of 10 minutes (i.e.,  $u' = u - \langle u \rangle$ ).

268 The swash excursion ( $S_x$ ) is computed along the central cross-shore swash



269 profile (at  $y = 120$  m), where water and bed level data are stored at high  
 270 frequency (2 Hz) and at 1 m intervals.  $S_x$  is taken as the difference between  
 271 the cross-shore position of the lower and upper level of the wet/dry interface  
 272 (at the 2<sup>nd</sup> and 98<sup>th</sup> percentiles, respectively) during successive 10-minute in-  
 273 tervals (n.b., a grid point is considered dry once  $h < 5$  cm). The swash height  
 274 ( $S_z$ ) is the corresponding difference between the lower and upper elevation  
 275 of the wet/dry interface during the same time interval. The swash slope ( $\beta$ )  
 276 is equal to  $S_z/S_x$ . Final values of  $S_x$  and  $S_z$  are extracted as the mean over  
 277 the 30-minute period before and after the time of the last mid-tide at 2.83  
 278 days.

279 Finally, the surface sediment composition,  $P_{D_{50}}$  is computed for case C4  
 280 (having a mixed sediment bed) as:

$$P_{D_{50}} = \frac{P_{c,t} - P_{c,i}}{P_{c,i}} \quad (4)$$

281 where  $P_c$  is the percentage of coarse sediment in the surface layer initially  
 282 (subscript  $i$ , and where  $P_{c,i} = 50\%$ ) or at any time during the simulation  
 283 (subscript  $t$ ). Thus,  $P_{D_{50}}$  values of 1, 0 and -1 indicate that the surface  
 284 sediment is 100% coarse, evenly mixed (50% coarse and 50% fine) and 100%  
 285 fine, respectively.

### 286 **3. Results**

#### 287 *3.1. Predicted Length Scales*

288 The final bathymetries for all 24 simulations (taken at the last mid-tide  
 289 level at 2.83 days) are shown in Fig. 4. The 14 simulations in Series A are  
 290 shown in Fig. 4a–n, the 6 simulations in Series B are shown in Fig. 4o–t,

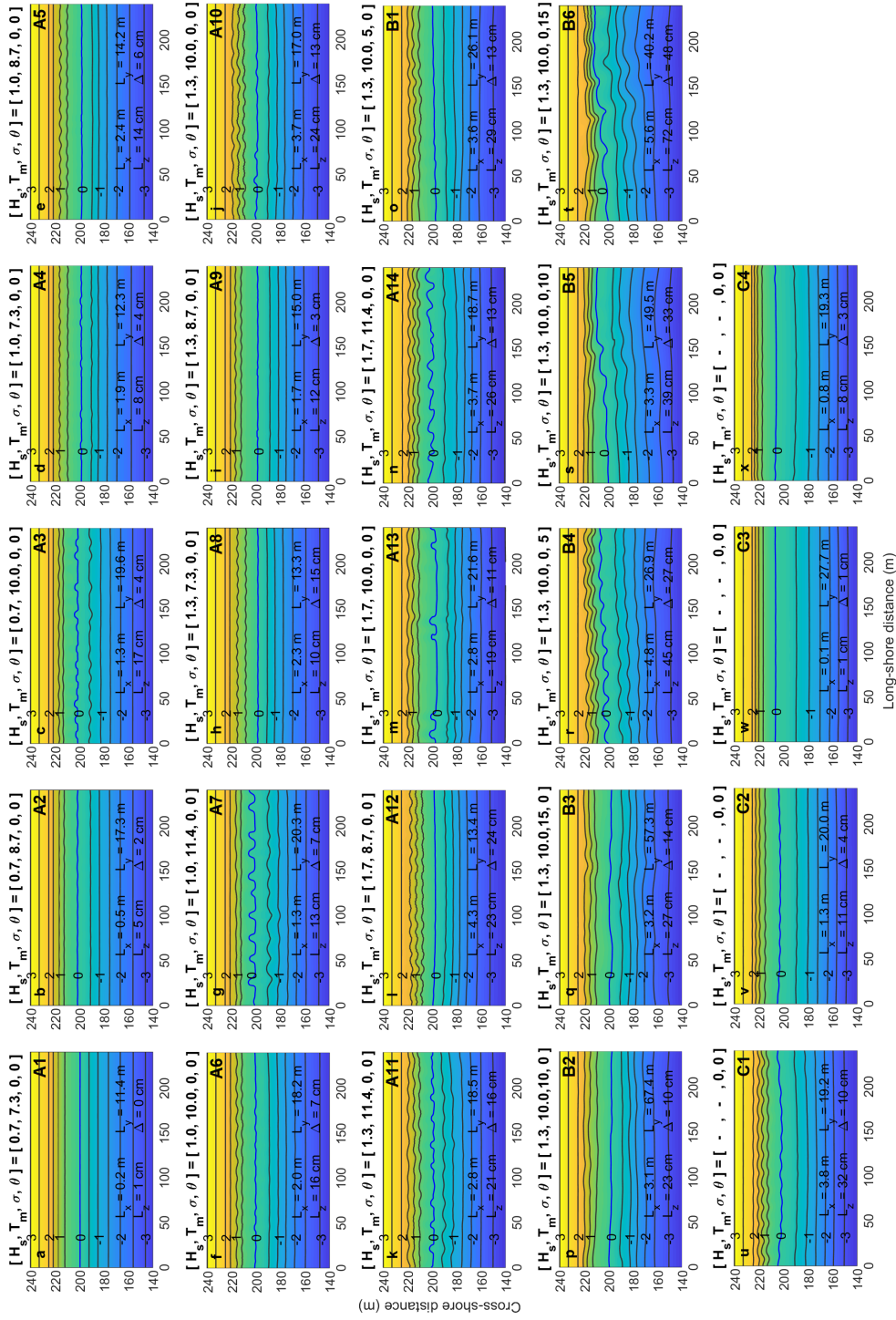


Figure 4: Bathymetry of the model domain extracted at the last mid-tide of the simulation ( $T = 2.83$  days) showing resulting cusped features and corresponding length scales. Panels a–t show results for simulations forced with synthetic wave conditions and u–x show those forced with actual wave data while varying  $D_{50}$ .

291 and finally, the 4 simulations in Series C are shown in Fig. 4u–x. Here, it is  
292 seen that cusps clearly develop for certain cases and are subdued for others.  
293 For the cases where cusps do form, they are generally located in a narrow  
294 area between 0 and 1.5 m elevation on the sub-aerial beach face. Prominent  
295 cusps are obtained for cases A10-14, B1, B4, B6 and C1. The only two cases  
296 where cusps did not form at all are A1 and C3.

297 The length scales of the cusps vary as they evolve, depending on the  
298 elevation of the tide and the movement of the swash zone up and down the  
299 beach face, as shown for the *base case* (A10) in Fig. 5a–f. Cusps generally  
300 begin to appear after the first tidal cycle with low  $L_z$  and  $\Delta$  values, which are  
301 then enhanced over the remaining two tidal cycles (Fig. 5e–f). At the end of  
302 the simulations, the level of the tide is low, leaving the upper beach exposed  
303 and morphologically inactive. It is at this moment (mid-tide occurring at 2.83  
304 days) that final values of  $L_x$ ,  $L_y$ ,  $L_z$ ,  $\Delta$  and  $AR$  are taken as representative  
305 of the response to the prescribed forcing conditions or sediment composition.

### 306 3.1.1. Series A: Varying $H_s$ and $T_m$

307 Fig. 4a–n shows prominent cusps develop for certain combinations of  
308  $H_s$ - $T_m$  (generally when  $H_s > 1.3$  m and  $T_m > 10$  s) and are subdued for  
309 others (generally when  $H_s < 1$  m and  $T_m < 10$  s). There is one case where  
310 beach cusps do not form at all (case A1), despite accretion of the beach face.  
311 Fig. 6a–d shows the resulting length scales for the simulations in Series A.  
312 For cases where cusps are present (A2 – A14),  $L_y$  varies between 12 – 22 m.  
313 Increases in  $T_m$  (for the same  $H_s$ ) generally results in increased  $L_y$  (warmer  
314 colours concentrated in top half of Fig. 6b).  $L_x$  and  $L_z$  increases with  
315 increasing  $H_s$  and, to a lesser extent, with  $T_m$  (warmer colours concentrated

<b>Run ID</b>	$H_s$ (m)	$T_m$ (s)	$\sigma$ (°)	$\theta$ (°)	$D_{50}$ (mm)	$L_x$ (m)	$L_y$ (m)	$L_z$ (cm)	$\Delta$ (cm)	$AR$ (-)
A1*	0.7	7.3	0	0	0.5	0.2	11.4	1	0	57
A2	0.7	8.7	0	0	0.5	0.5	17.3	5	2	35
A3	0.7	10.0	0	0	0.5	1.3	19.6	17	4	15
A4	1.0	7.3	0	0	0.5	1.9	12.3	8	4	6.5
A5	1.0	8.7	0	0	0.5	2.4	14.2	14	6	5.9
A6	1.0	10.0	0	0	0.5	2.0	18.2	16	7	9.1
A7	1.0	11.4	0	0	0.5	1.3	20.3	13	7	16
A8	1.3	7.3	0	0	0.5	2.3	13.3	10	15	5.8
A9	1.3	8.7	0	0	0.5	1.7	15.0	12	3	8.8
<b><u>A10</u></b>	<b>1.3</b>	<b>10.0</b>	<b>0</b>	<b>0</b>	<b>0.5</b>	<b>3.7</b>	<b>17.0</b>	<b>24</b>	<b>13</b>	<b>4.6</b>
<u>A11</u>	1.3	11.4	0	0	0.5	2.8	18.5	21	16	6.6
<u>A12</u>	1.7	8.7	0	0	0.5	4.3	13.4	23	24	3.1
<u>A13</u>	1.7	10.0	0	0	0.5	2.8	21.6	19	11	7.5
<u>A14</u>	1.7	11.4	0	0	0.5	3.7	18.7	26	13	5.1
<u>B1</u>	1.3	10.0	5	0	0.5	3.6	26.1	29	13	7.3
B2	1.3	10.0	10	0	0.5	3.1	67.4	23	10	22
B3	1.3	10.0	15	0	0.5	3.2	57.3	27	14	18
<u>B4</u>	1.3	10.0	0	5	0.5	4.8	26.9	45	27	5.6
B5	1.3	10.0	0	10	0.5	3.3	49.5	39	33	15
<u>B6</u>	1.3	10.0	0	15	0.5	5.6	40.2	72	48	7.1
<u>C1</u>	varies	varies	0	0	0.5	3.8	19.2	32	10	5.1
C2	varies	varies	0	0	0.3	1.3	20.0	11	4	15
C3*	varies	varies	0	0	0.2	0.1	27.7	1	1	277
C4	varies	varies	0	0	0.5/0.2	0.8	19.3	8	3	24

Table 3: Simulation Results (base case in bold; case names featuring prominent cusps underlined; \* no cusps formed)

316 in the top right of Fig. 6a and c). And finally, increased  $\Delta$  values are  
317 generally associated with larger  $H_s$  (warmer colours concentrated on right

318 side of Fig. 6d).

### 319 3.1.2. Series B: Varying $\sigma$ and $\theta$

320 Fig. 6e–h shows the response values of cusp length scales to changes in  
321  $\sigma$  and  $\theta$ . Increasing values of  $\sigma$  and  $\theta$  from 0 produce large increases in  
322  $L_y$ , with values ranging between 26 – 67 m. This is a significant increase  
323 in  $L_y$  compared to the base case, where  $L_y$  is 17 m. This may be explained  
324 by the increased long-shore width of the swash trajectory (i.e. the path a  
325 water particle traces during swash and backwash, distinct from  $S_x$ ) for higher  
326 values of  $\sigma$  and  $\theta$ . It is important to also note in Fig. 4 that for cases where  
327  $\theta$  is varied, the resulting cusps are saw-toothed shaped due to the asymmetry  
328 of the swash trajectory. This is not seen in the cases where  $\sigma$  is varied, as  
329 the swash trajectory is symmetrical about the shore normal. For increased  
330  $\sigma$ ,  $L_x$  tends to slightly decrease while  $L_z$  and  $\Delta$  remain fairly stable. For  
331 increased  $\theta$ ,  $L_x$ ,  $L_z$  and  $\Delta$  tend to increase.

### 332 3.1.3. Series C: Time-varying wave conditions

333 Case C1, run with measured wave data and the native sediment size of  
334 0.5 mm, produced prominent cusp patterns with  $L_x$  and  $L_y$  equal to 3.8  
335 and 19.2 m, respectively. Cusp patterns also emerge much earlier (after  $\sim 3$   
336 hours) than the simulations with constant wave forcing (which consistently  
337 appear only after  $\sim 18$  hours, e.g. Fig. 5e–f), as the wave conditions regularly  
338 change with time. The beach cusps themselves are also more dynamic, with  
339 greater long-shore migration observed in contrast to relatively static cusps in  
340 the simulations with constant wave forcing. For the remaining cases, cusps  
341 are either weakly defined (C2 and C4) or non-existent (C3). For the latter

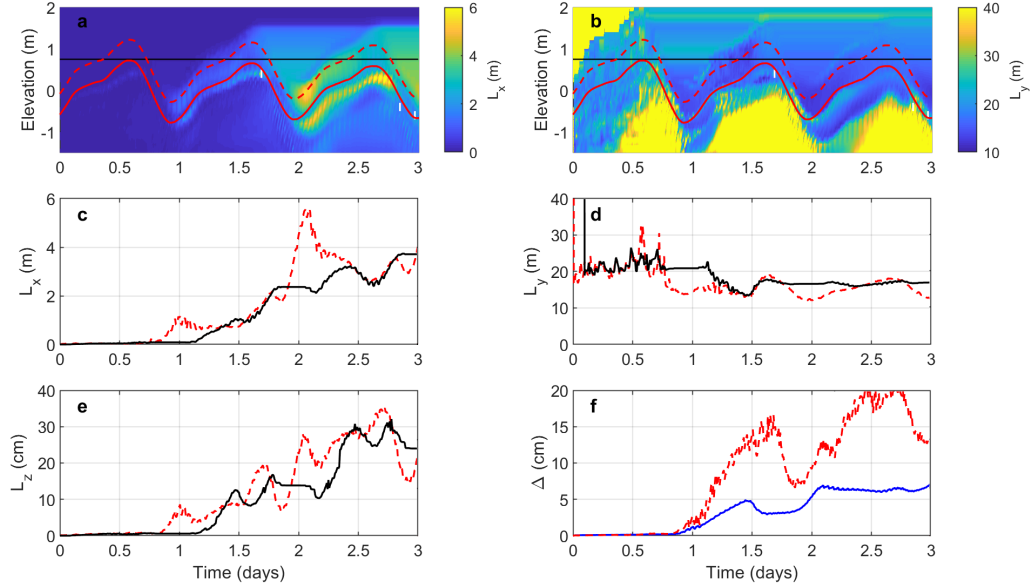


Figure 5: Evolution of beach cusp length scales for the base case simulation. (a–b) Variation of  $L_x$  (a) and  $L_y$  (b) as a function of time and elevation relative to MSL. The solid red line indicates the height of the tide (near the lower limit of the swash) and the dashed red line shows (approximately) the mid- to upper-limit of the swash at 0.5 m above the tide level. The solid black line shows the maximum tide level of 0.75 m elevation. Changes in  $L_x$  and  $L_y$  occur as the swash zone moves up and down the beach face. At low tide (at time = 1, 2 and 3 days), the upper beach is dry and morphologically inactive. Data in areas above the tide level are associated with beach cusps, while data below tide level are associated with underwater bedform features. (c–f) Changes in  $L_x$ ,  $L_y$ ,  $L_z$  and  $\Delta$  as a function of time, respectively. The dashed red line and solid black lines correspond to those defined in (a–b). The solid blue line in (f) is the average  $\Delta$  taken between 0.5 and 1 m elevation.  $L_x$ ,  $L_z$  and  $\Delta$  remain low during the first tidal cycle as the planar beach begins to react to the imposed forcing conditions. They subsequently increase over the remaining two tidal cycles.

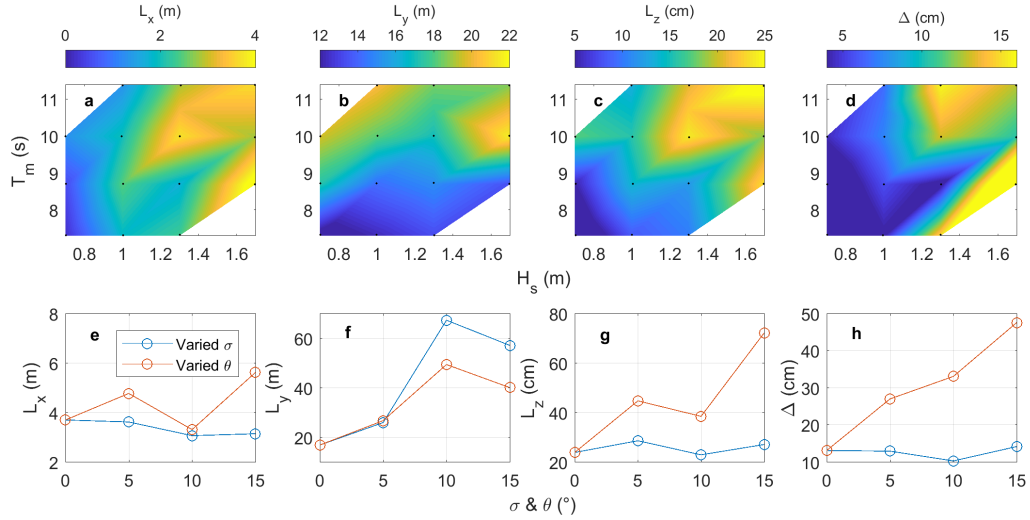


Figure 6: Resulting length scales of  $L_x$ ,  $L_y$ ,  $L_z$  and  $\Delta$  for different combinations of wave conditions in the  $H_s$ - $T_m$  parameter space (panels a–d) and, separately, in the  $\sigma$  and  $\theta$  parameter space (panels e–h). Black dots in panels (a–d) indicate the location of data points. Note further that the legend in panel (e) also applies to panels (f–h).

342 (C3), the finer sediment size of 0.2 mm causes the beach to strongly erode  
 343 under the same wave conditions at case C1.

344 When the sediment size is decreased to 0.3 and 0.2 mm (cases C2 and C3,  
 345 respectively), the upper beach no longer accretes, but is rather eroded to form  
 346 a low tide terrace (wide shallow area around MSL in Figure 4 v–x). Cuspate  
 347 features can still be discerned for in the pattern of erosion for the case C2,  
 348 however the beach is featureless for case C3 as the wave conditions are highly  
 349 erosive for the fine sediment, resulting in a dissipative beach profile.

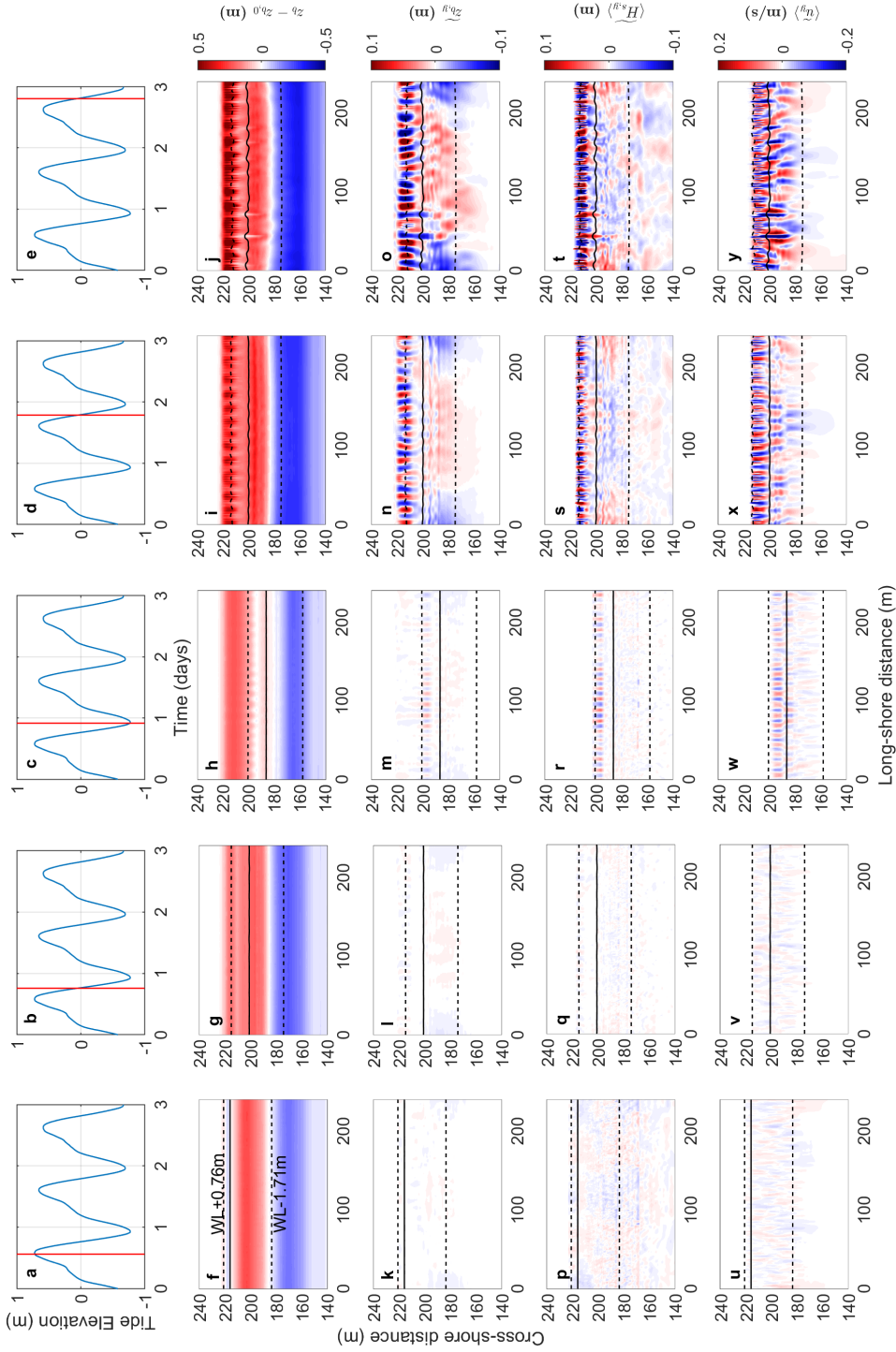


Figure 7: Temporal development of cusped morphology for the base case simulation (A10) shown during the first falling tide (high tide, mid-tide and low tide in columns 1-3, respectively) and for the last two mid-tides (columns 4-5). Rows 1 to 5 show the tide elevation, cumulative erosion/sedimentation pattern,  $\langle \tilde{z}_{b,y} \rangle$ ,  $\langle \tilde{H}_{s,y} \rangle$ , and  $\langle \tilde{u}_y \rangle$ , respectively.



350 *3.2. Temporal Evolution and Swash Dynamics*

351 *3.2.1. Temporal development of cusps*

352 Fig. 7 shows the temporal evolution of cusped morphology for the base  
353 case simulation (A10), which is fairly representative for all the other cases  
354 considered. During the initial rising tide, small alternating perturbations  
355 in the wave and current field are observed. The perturbations are, how-  
356 ever, too small cause any significant variation in  $\langle \widetilde{H}_{s,y} \rangle$  or  $\langle \widetilde{u}_y \rangle$ , therefore  
357 the bathymetry is slow to respond. Nonetheless, during this initial period,  
358 sediment is slowly moved onshore, just below the tide level (Fig. 7f). This  
359 subaqueous mass of accreted sediment becomes exposed when the tide turns  
360 after the first high tide. It is reworked and sediment is freshly deposited at  
361 the top of the swash as the water level recedes, creating a berm (Fig. 7g).  
362 This trail of sediment is slowly sculpted into small cusped features as sed-  
363 iment deposition becomes irregular long-shore. By the start of the second  
364 tidal cycle, these remnant cusped perturbations,  $\widetilde{z}_{b,y}$ , begin to amplify the  
365 wave height pattern to a sufficient degree to cause notable variations in  $\langle \widetilde{H}_{s,y} \rangle$   
366 and  $\langle \widetilde{u}_y \rangle$ , which further enhances  $\widetilde{z}_{b,y}$  through positive feedback. Over time,  
367 these feedbacks allow the cusp dimensions to steadily increase over time,  
368 particularly  $L_x$ ,  $L_z$  and  $\Delta$  (as shown in Fig. 5).

369 For all simulations, the  $\langle \widetilde{H}_{s,y} \rangle$  pattern is consistently negatively correlated  
370 with  $\widetilde{z}_{b,y}$  ( $-0.33 > r > -0.64$ , averaged over last tidal cycle), with both  
371 patterns developing simultaneously. This indicates that wave heights are  
372 higher on the cusp horns and smaller in the troughs. Simulations in which  
373 the cusp field does not clearly materialize are those in which accretion is not  
374 particularly strong during the initial (and subsequent) tidal cycles, especially

375 in the upper part of the beach. The cusp field also does not fully develop in  
376 simulations where the pattern of  $\langle \widetilde{H_{s,y}} \rangle$  or  $\langle \widetilde{u_y} \rangle$  is not strongly perturbed.

### 377 3.2.2. TKE and swash flow patterns

378 The variation of  $k$  along the central cross-shore transect allows us to see  
379 areas where wave-breaking-induced turbulence is strongest. The left panels in  
380 Fig. 8 show that  $k$  is maximum in the inner surf zone during the falling tide,  
381 maximum in the swash around high tide. Greater levels of swash turbulence  
382 around high tide (where cusps are to be found) is observed for increasing  
383  $H_s$ ,  $\sigma$  and  $\theta$ . Swash flow patterns (10-minute time-averaged  $\langle u \rangle$  and  $\langle v \rangle$   
384 velocities) are generally found to be horn-divergent and symmetric for cases  
385 in Series A (normally incident waves), with flow converging in the trough of  
386 the cusp and with strong return currents (Fig. 8b and d). These flow patterns  
387 become asymmetric and elongated long-shore in the inner surf and swash for  
388 slightly increased  $\theta$  (e.g. case B4, Fig. 8f). The increased turbulence for  
389 small increases of  $\sigma$  and  $\theta$  beyond normal (i.e.  $> 0^\circ$ ) potentially amplifies  
390 cusp dimensions, but may prove to be too dynamic for larger values above  
391 normal. Fig. 8g and h show, for case B3,  $k$  values are consistently high in the  
392 surf and for longer periods in the swash around high tide compared to the  
393 base case. The resulting mean flow pattern lacks the rhythmicity observed  
394 in the base case, with more uniform cross-shore flow.

### 395 3.2.3. Swash Excursion, Height and Slope

396 Fig. 9 shows  $S_x$ ,  $S_z$  and  $\beta$  for the base case simulation, which has similar  
397 results as most other cases. As seen in Fig. 9b,  $\beta$  and tide elevation are  
398 positively correlated, varying at the same timescale (i.e., the beach is steeper

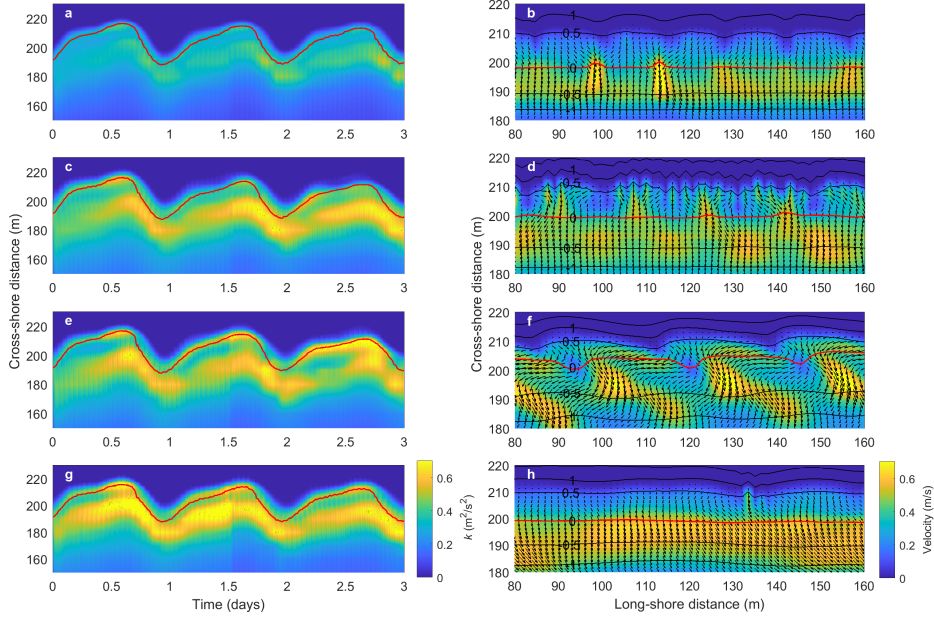


Figure 8: (Left panels) Temporal variation of turbulent kinetic energy ( $k$ ) along the central cross-shore transect ( $y = 120$  m) for cases A5, A10 (base case), B4 and B3 (panels a, c, e, and g, respectively). Red line indicates tide level. (Right panels) Spatial variation of the mean swash velocity field (combined  $\langle u \rangle$  and  $\langle v \rangle$ ) taken around the last mid-tide level ( $T = 2.83$  days) for cases A5, A10 (base case), B4 and B3 (panels b, d, f, and h, respectively). Red line indicates shoreline (0 m contour level), and black lines show contour levels above and below spaced 0.5 m.

399 around high tide and more gently sloping around low tide).  $S_x$  is consistently  
 400 negatively correlated with the swash slope and tide elevation above MSL (i.e.,  
 401  $S_x$  is smallest around high tide, where the beach slope is steepest). In some  
 402 cases,  $S_x$  is maximum at low tide while in others  $S_x$  is maximum just below  
 403 mid-tide and subsequently decreases towards low tide (Fig. 9c). The latter  
 404 is due to a berm forming at the low tide level that increases  $\beta$  around that  
 405 section of the beach profile.  $S_x$  and  $S_z$  increases, as expected, with increased

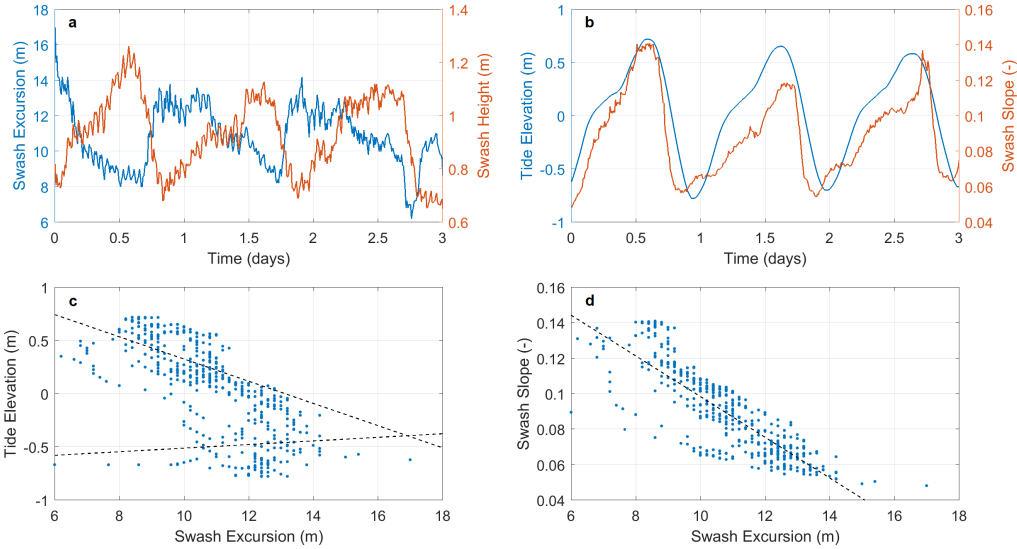


Figure 9: (Top panels) Temporal variation of swash excursion and swash height (a), and tide elevation and swash slope (b). (Bottom panels) Scatter plots of tide elevation (c) and swash slope (d) against swash excursion. Lines of best fit (black, dashed) are shown in (c) for data above and below -0.1 m tide elevation, and in (d) for all data.

406  $H_s$ . For the base case (A10), the swash excursion generally ranges between 6–  
 407 16 m; and for case C1 it ranges between 8–20m. At the end of the simulation,  
 408  $S_x$  measures 9.5 m for case A10 and 13.9 m for case C1.

### 409 3.3. Surface Sediment Composition

410 The final simulation (case C4) shows the effect of varying the sediment  
 411 composition by including two classes of sediment (fine and coarse) in the  
 412 surface and under layers. Both classes are equally distributed in the sedi-  
 413 ment bed at the start of the simulation; however as time passes, the surface  
 414 sediment composition ( $P_{D_{50}}$ ) changes. The finer sediment fraction is gen-  
 415 erally displaced from the swash zone and deposited on the low tide terrace

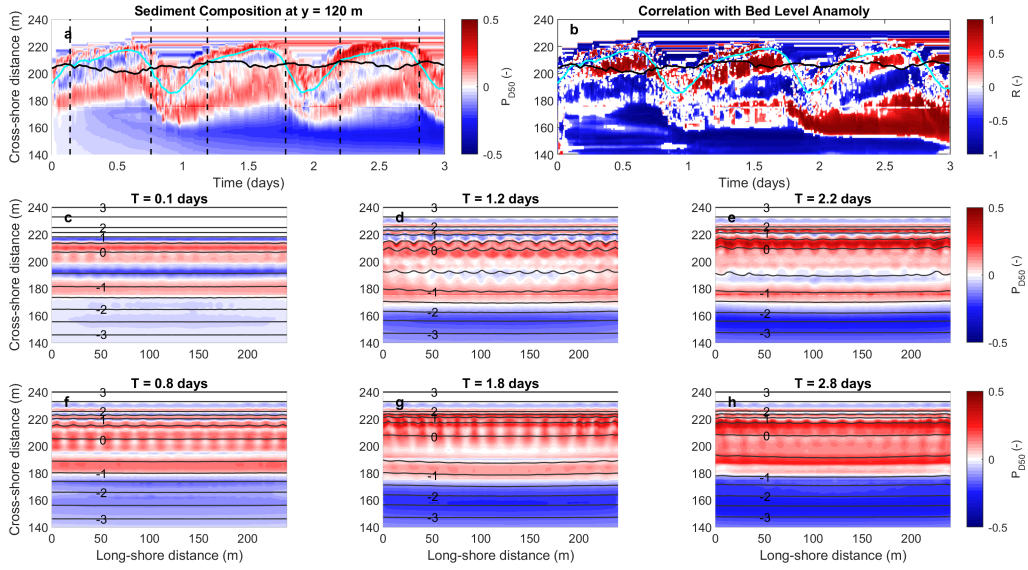


Figure 10: (a-b) Temporal evolution of (a) surface sediment composition ( $P_{D_{50}}$ ) along the central cross-shore profile ( $y = 120$  m), and (b) the correlation between  $P_{D_{50}}$  and  $\widetilde{z_{b,y}}$ . Solid black and blue lines show the time-varying movement of the cross-shore position of the shoreline ( $z = 0$  m) and the tide water level, respectively. (c-h) Spatial variation of  $P_{D_{50}}$  at (c-e) mid-tide level on a rising tide and (f-h) mid-tide level on a falling tide. Dashed black lines in (a) indicate the times when (c-h) are shown. Black lines in (c-h) indicate bed level contours drawn at 0.5 m intervals. The colour scale in (a, c-h) is white (values near 0) for an evenly mixed bed (50% coarse and 50% fine sediment). Red colours (positive values up to 1) indicate a greater presence of coarser sediment, and vice versa for blue colours (negative values down to -1). Finally, the color scale in (b) is white (values near 0) when there is no correlation between  $P_{D_{50}}$  and  $\widetilde{z_{b,y}}$ . Red colours indicate there is a positive correlation (coarser sediment located on cusp horn), and vice versa for blue colours (coarser sediment located in cusp trough).

416 while the coarser sediment fractions armour the swash (Fig. 10c-h). Despite  
 417 this, there are still times when fine sediment will be pushed back into the  
 418 surf zone during the rising tide (Fig. 10a); therefore, there is still a mixture

419 of fine and coarse sediment in the surf zone over time. This mixture of fine  
420 and coarse sediment creates a pattern surrounding the cusp field with similar  
421 length scales as  $\widetilde{z}_{b,y}$  (which identifies the cusp horns and troughs); therefore,  
422 it is possible to investigate their long-shore correlation. This result is shown  
423 in Fig. 10b, where temporal patterns of strong positive (and negative) cor-  
424 relations can be seen. Positive (negative) correlations shown in red (blue)  
425 indicate times when coarser sediment is found on the horn (trough) of the  
426 cusps. The pattern of correlation fluctuates with tidal elevation but is gen-  
427 erally positively correlated around the time-varying water level (i.e. coarser  
428 sediment located on the horn). Nonetheless, there are times when the ex-  
429 posed sediment composition pattern shows that coarser sediment is located  
430 in the trough of the cusp rather than on the crest (e.g. the upper beach  
431 during the second low tide).

## 432 4. Discussion

### 433 4.1. Evaluation of Length Scales

#### 434 4.1.1. Comparison to Measurements at Nha Trang Beach

435 As we have used conditions representative of the situation at Nha Trang  
436 Beach as the basis of our simulations, we therefore look to compare simulated  
437 values of  $L_y$  to what was actually measured (28 m). Hardly any of the cases in  
438 Series A come close, with mean  $L_y$  of 16.5 m and maximum of 21.6 m. Even  
439 case C1, run with measured  $H_s$  and  $T_m$  values, underestimates the measured  
440 value by almost a third, with a final  $L_y$  of 19.2 m. However, it should  
441 be noted that simulations in Series A and Series C are run with normally  
442 incident waves without directional spreading. However, we have seen from

443 Series B that accounting for slight increases in  $\sigma$  and  $\theta$  would result in larger  
444 values of  $L_y$  (cases B1 and B4) that are more comparable to the measured  
445 value ( $L_y > 26$  m). Simulated values of  $\beta$  in the base case and case C1 follow  
446 similar trends as the measurements, being steepest around high tide and vice  
447 versa around low tide. The range of simulated values are also around the  
448 same range as the measurements, between 0.04 and 0.12.  $S_x$  tends to be  
449 maximum at low tide in the simulations (where  $\beta$  is lowest) while, on the  
450 other hand, it is maximum around high tide in the measured data (where  $\beta$   
451 is highest).

452 If we consider the average wave conditions (defined by  $H_s$  and  $T_m$ ) for  
453 case C1 during the 3-day simulation period (approximately 1.17m and 10 s,  
454 respectively), it would fall between the time-constant forcing values of case  
455 A6 and A10. Wave conditions peaked during the first tide cycle (1.4 m and  
456 11.5 s, similar to case A11), and were lowest during the last tidal cycle (1.0  
457 m and 8.5 s, similar to case A5). The cusps produced at the end of the  
458 simulation in C1 are of similar magnitude as case A6, A10 and A11 (mid-  
459 to high-end of the wave conditions). After being formed during the first tide  
460 cycle,  $L_y$  did not adapt to the smaller dimensions expected during the lower  
461 energy conditions (shown for case A5). Instead,  $L_y$  remains fairly constant  
462 as energy levels fall, as also observed in the field. Thus, the sequencing of  
463 wave conditions can affect resultant cusp spacing, as commonly noted in the  
464 field where pre-existing cusp formations may persist for some time before  
465 newer cusp fields are able to develop, largely depending on how quickly and  
466 to what degree actual wave conditions change (van Gaalen et al., 2011).

467 Finally, we note that  $L_y$  does not vary significantly between high and

468 mid-tide in our simulations or from the observations at Nha Trang Beach,  
 469 perhaps due to the micro-tidal environment. Nolan et al. (1999) were able  
 470 to show a dependence of  $L_y$  on elevation above MSL; however, their study  
 471 site was located in a meso-tidal environment (2.6 m range) exposed to more  
 472 energetic wave conditions.

#### 473 4.1.2. Comparison to Empirical and Theoretical Formulae

474 Empirical equations for predicting  $L_y$  have been developed based on field  
 475 observations. One such by Sunamura (2004) uses the sediment diameter  
 476 ( $D_{50}$ ), wave period, wave height, and gravitational acceleration ( $g$ ) as depen-  
 477 dent variables, given as:

$$L_{y,Sun} = A \exp(-0.23 D_{50}^{0.55}) T \sqrt{gH} \quad (5)$$

478 where  $A$  is a scaling factor ranging from  $\sim 0.65$  for laboratory cases to  $\sim 1.35$   
 479 for field cases. Expected values of  $L_y$  may also be calculated based on both  
 480 the self-organisation and edge wave generation theories, shown, respectively,  
 481 in Eq. 6 and Eq. 7 following as:

$$L_{y,SO} = f S_x \quad (6)$$

$$L_{y,EW} = \frac{g T_i^2}{m \pi} \sin \beta \quad (7)$$

482 where  $f$  is a factor generally taken to be 1.63 (but which may range between  
 483 1 and 3);  $S_x$  is the swash excursion;  $m$  is a factor equal to 1 and 2 for sub-  
 484 harmonic ( $L_{y,Sub}$ ) and synchronous ( $L_{y,Syn}$ ) edge waves, respectively;  $\beta$  is the  
 485 beach slope; and  $T_i$  is the incoming wave period (Coco et al., 1999). Results



486 are shown in Table 4 for final values of  $S_x$  for each simulation (extracted  
 487 from the model output around  $T = 2.83$  days, as mentioned in § 2.3.3), from  
 488 which final values of  $\beta$  and  $f$  are computed (with  $f$  being the ratio  $L_y/S_x$ ).  
 489 Values of  $L_{y,Sub}$ ,  $L_{y,Syn}$ ,  $L_{y,SO}$ , and  $L_{y,Sun}$  are also shown for comparison  
 490 with Series A. It should be noted that some scatter is expected in our data  
 491 as we are unable to control exactly where along a cusp (between the horn  
 492 and trough)  $S_x$  and  $\beta$  are extracted, as the exact position of cusps at the  
 493 central cross-shore profile varies during the course of the simulation for each  
 494 case.

495 When using Eq. 5 to compute  $L_{y,Sun}$  in Table 4, we computed and used  
 496 the value of  $A$  that minimised the root-mean-square error (the best-fit value)  
 497 between  $L_{y,Sun}$  and  $L_y$ , which was equal to 0.6 – very close to the value of  
 498 0.65 reported in Sunamura (2004). Values of  $L_{y,Sun}$  are not much different  
 499 to the simulation results of Series A, with raw error around 14% on average.  
 500 Applying Eq. 5 to the average measured wave conditions (1 m, 9 s) and  
 501 using the field value of  $A = 1.35$ , we obtain a predicted value of  $L_{y,Sun}$  of  
 502 32 m, a slight over-prediction. Thus, Eq. 5 predicts  $L_y$  reasonably well for  
 503 both Series A (laboratory-type cases which have no directional spreading  
 504 and normally incident waves) and for the actual field case at Nha Trang  
 505 Beach. For Series B, where  $\theta$  and  $\sigma$  are increased, using  $A = 0.6$  largely  
 506 underestimates  $L_y$ . The estimate is improved when using  $A = 1.35$ , with  
 507 a best-fit value of 1.7. Sunamura (2004) noted the large difference between  
 508  $A$  obtained for laboratory and field data, attributing the larger field value  
 509 to irregular wave forcing in the field. However, it should also be noted that  
 510 slight increases in  $\theta$  and  $\sigma$  in Series B also enhanced  $L_y$ , which may also help

511 to account for the larger  $A$  values of field cases, since there is at least some  
512 degree of directional spreading expected.

513 Table 4 shows that simulated  $\beta$  and  $f$  generally increase with  $H_s$  and  $T_m$ .  
514 With regard to  $f$ , the simulation results ranges from 1.16 to 2.47, which fits  
515 within the range of expected  $f$  values (1 to 3). The best-fit value of  $f$  is  
516 found to be 1.63 – equal to that reported in Coco et al. (1999). As  $f$  varies  
517 according to specific forcing conditions, values of  $L_{y,SO}$  overestimate  $L_y$  at  
518 low  $H_s$  and  $T_m$  values (such as case A1 or A4) and vice versa at high  $H_s$  and  
519  $T_m$  values (such as case A11 or A14). Almar et al. (2008) and Vousdoukas  
520 (2012) have reported observed mean  $f$  values of 1.69 and 3.47, respectively,  
521 under average wave conditions of  $[H_s, T_m] = [1.5 \text{ m}, 10 \text{ s}]$  at Tairua Beach  
522 (former), and  $= [1 \text{ m}, 8 \text{ s}]$  at Faro Beach (latter). While the observed  $f$ -value  
523 of Almar et al. (2008) is not much different with our findings from Series A  
524 ( $\theta$  is reported to be almost always shore normal), that of Vousdoukas (2012)  
525 is much larger than expected. For the latter, it is important to note that  
526 there were large variations of measured  $\theta$  values, up to  $40^\circ$ . This may help to  
527 explain why the observed  $L_y$  (on average 50 m) is quite large in comparison  
528 to the measured  $S_x$ . As seen from our simulations, for  $\theta \geq 10^\circ$  (cases B5  
529 and B6) we obtain mean  $f$  values of 5.8 and  $L_y$  of 45 m – comparable to  
530 Vousdoukas (2012).

531 Regarding the synchronous edge wave theory,  $L_{y,Syn}$  significantly underes-  
532 timates  $L_y$  for cases with lower  $H_s$  and  $T_m$  values (for cases A1–A5, around  
533 48% lower) and vice versa at high  $H_s$  and  $T_m$  values (for cases A10–A14,  
534 around 12% higher). Alternatively, for sub-harmonic edge waves,  $L_{y,Sub}$   
535 slightly overestimates  $L_y$  for cases with lower  $H_s$  and  $T_m$  values (for cases

<b>Run ID</b>	$S_x$ (m)	$\beta$ (-)	$f$ (-)	$L_y$ (m)	$L_{y,Sub}$ (m)	$L_{y,Syn}$ (m)	$L_{y,SO}$ (m)	$L_{y,Sun}$ (m)
A1	9.8	0.044	1.16	11.4	10.2	5.1	16.0	9.8
A2	9.3	0.052	1.85	17.3	17.1	8.5	15.2	11.7
A3	8.5	0.055	2.29	19.6	24.0	12.0	13.9	13.4
A4	10.0	0.055	1.23	12.3	12.7	6.3	16.3	11.7
A5	12.0	0.048	1.18	14.2	15.9	8.0	19.6	14.0
A6	8.3	0.071	2.19	18.2	30.7	15.4	13.6	16.1
A7	8.2	0.078	2.47	20.3	44.1	22.1	13.4	18.3
A8	11.4	0.056	1.17	13.3	13.0	6.5	18.5	13.4
A9	9.6	0.072	1.56	15.0	23.8	11.9	15.7	15.9
A10	9.5	0.075	1.80	17.0	32.5	16.2	15.4	18.3
A11	8.5	0.094	2.17	18.5	53.2	26.6	13.9	20.9
A12	9.9	0.081	1.36	13.4	26.8	13.4	16.1	18.2
A13	12.2	0.083	1.77	21.6	36.1	18.0	19.8	20.9
A14	11.1	0.092	1.69	18.7	51.9	25.9	18.0	23.9
B1	12.5	0.066	2.08	26.1	–	–	–	–
B2	11.9	0.064	5.66	67.4	–	–	–	–
B3	13.9	0.061	4.12	57.3	–	–	–	–
B4	8.1	0.115	3.33	26.9	–	–	–	–
B5	7.3	0.098	6.79	49.5	–	–	–	–
B6	8.4	0.096	4.80	40.2	–	–	–	–
C1	13.9	0.059	1.39	19.2	–	–	–	–
C2	13.5	0.060	1.48	20.0	–	–	–	–
C3	13.2	0.063	2.10	27.7	–	–	–	–
C4	14.9	0.083	1.29	19.3	–	–	–	–

Table 4: Simulation results of  $S_x$ ,  $\beta$ ,  $f$  and  $L_y$  for Series A, B and C, with Series A compared with expectations from the edge wave (sub-harmonic and synchronous) and self-organisation theories, and Sunamura (2004) ( $L_{y,Sub}$ ,  $L_{y,Syn}$ ,  $L_{y,SO}$  and  $L_{y,Sun}$ , respectively).

536 A1–A5, around 5% lower) but severely overestimates  $L_y$  at high  $H_s$  and  
 537  $T_m$  values (for cases A10–A14, around 125% higher). Similar findings are  
 538 shown in Dodd et al. (2008), though only  $T_m$  was varied in their simulations.  
 539 Therefore,  $L_{y,sub}$  predictions would appear to be suited to low wave energy  
 540 conditions and those for  $L_{y,syn}$  to higher energy conditions; but neither are  
 541 very good predictors across the board when compared to  $L_y$ . Guza and In-  
 542 man (1975) note that sub-harmonic edge waves are more easily generated  
 543 than synchronous edge waves, and that both are not generally found under  
 544 energetic wave conditions, where the high turbulence of plunging breakers  
 545 disrupts their excitation. The generation of certain types of edge waves in  
 546 itself is also highly dependent on, *inter alia*, beach topography, frequency  
 547 spread of incident waves, and dissipation by waves and currents. Therefore  
 548 it is not clear which edge wave mode is best suited for comparison to  $L_y$ .  
 549 Indeed in the literature, comparisons between measured data and theoretical  
 550 edge wave predictions vary widely from being strongly to weakly correlated  
 551 (Kaneko, 1985; Rasch et al., 1993; Almar et al., 2008) and even distinguishing  
 552 between different modes of edge waves may be difficult in reality (Holland  
 553 and Holman, 1996). Nevertheless, it may be possible to identify edge waves  
 554 using XBeach (whether synchronous or sub-harmonic) from seaward radiat-  
 555 ing wave reflection patterns. As shown in Fig. 7, a pattern of alternating  
 556 perturbations in  $\langle \widetilde{H_{s,y}} \rangle$  is seen during the initial development of cusps, obvi-  
 557 ously caused by the interaction between incoming and reflected waves (similar  
 558 to Almar et al. (2018)). However, our model output is not saved at a high  
 559 enough frequency to separate incoming from reflected waves, and we are thus  
 560 unable to definitively quantify the presence of edge waves. Nonetheless, this

561 may be looked at in greater detail in future work that is more focused on  
562 mechanisms surrounding cusp initiation.

#### 563 *4.2. Evaluation of development, circulation and sediment patterns*

564 TKE ( $k$ ) is shown to be maximum in the swash around high tide (Fig.  
565 8a, c, e, g) where the swash slope tends to be steepest (9b). Wave heights in  
566 the swash are also highest around high tide (c.f. Fig. 5 in Daly et al. (2017)).  
567 We see that moderate amounts of swash zone turbulence ( $0.3\text{--}0.5\text{ m}^2/\text{s}^2$ ) suf-  
568 ficiently mobilizes sediment, stimulating morphodynamic feedbacks leading  
569 to cusp development. This explains why cusps generally form around 1 m  
570 elevation (around the high tide level) in our simulations, even in cases where  
571 they are barely discernible. Dubois (1981) also observed that the elevation  
572 of cusps on the beach face was controlled by the elevation of swash run-up  
573 associated with wave conditions over the tidal cycle, particularly at high tide.

574 We have shown in our simulations that increased  $T_m$  generally results in  
575 increased  $L_y$ . Longer intervals between swash events for higher period waves  
576 would tend to reduce bore (swash-swash) interactions occurring on the beach-  
577 face, allowing stronger return flow during the backwash capable of sculpting  
578 wider cusps. Dodd et al. (2008) obtained similar results, and showed that  
579 the swash period may resonate with the incoming wave period to enhance  
580 backwash. Our simulations also showed that increased  $H_s$  leads to larger  
581  $L_x$  and  $L_z$ , most likely caused by greater turbulence in the swash capable  
582 of reworking sediment into deeper and wider cusp features. All simulations  
583 with developed cusps featured horn-divergent flow patterns, as is commonly  
584 observed in the field (Masselink and Pattiaratchi, 1998b; Holland, 1998) and  
585 predicted by other numerical studies (Dodd et al., 2008).

586 Cusp dimensions are enhanced when  $\sigma$  (under normally incident waves)  
587 or  $\theta$  are low ( $\sim 5^\circ$ ). Larger values are shown to cause increased turbulence in  
588 the swash, which acts to inhibit cusp growth. Increased turbulence may be  
589 due to the effect of greater swash-swash interactions ( $\sigma > 0$ ) or asymmetric  
590 swash flow ( $\theta > 0$ ). Obliquely incident waves of  $20^\circ$  have been observed  
591 in the field to flatten cusped features (Masselink and Pattiaratchi, 1998a).  
592 Holland (1998) also noted that cusps are rarely observed, and tend to be  
593 destroyed, for angles of incidence greater than  $12^\circ$ . Holland (1998) suggests  
594 that as  $\theta$  increases, long-shore currents increasingly disrupt the cross-shore  
595 flow structure needed to form and maintain cusps. In our simulations where  
596  $\theta$  is varied, only case B4 resulted in a prominent cusp shape. While B5 and  
597 B6 do produce shoreline undulations, they have high aspect ratios which  
598 diminish their prominence.

599 In terms of the sediment sorting pattern around cusps, by looking at the  
600 correlation between  $P_{D_{50}}$  and  $\widetilde{z}_{b,y}$  in Fig. 10b, we showed that sediment is  
601 generally coarser on the horns than in the trough of the cusps. This is true  
602 for most field observations, such as Antia (1987) and Sallenger (1979) who  
603 also explains that, as swash flow is more powerful than backwash and as flow  
604 is generally horn divergent, fine sediment is removed from the horn (leaving  
605 coarser sediment behind) and deposited in the trough.

606 The effect of varying sediment size, by decreasing  $D_{50}$ , we obtain slight  
607 increases in  $L_y$ , as noted in Sunamura (2004). However, it comes at the  
608 expense of increasing the erodability of the beach (i.e. more dissipative),  
609 making cusps less prominent. In fact, case C3 the final profile is generally  
610 devoid of any shoreline features. The present results therefore show cusps

611 tend to form under accretive and mildly erosive conditions on coarse grained  
612 intermediate beaches, consistent with field observations (Holland, 1998; van  
613 Gaalen et al., 2011). Antia (1987) notes that while cusps may form on typ-  
614 ically dissipative beaches, they only appear during low energy events which  
615 may permit a temporary reflective beach state to form.

#### 616 *4.3. XBeach Sediment Transport Module*

617 The simulations have been done using the non-hydrostatic wave solver  
618 in XBeach while enabling sediment transport. This is quite experimental,  
619 as the sediment transport equations only account for transport due to flow  
620 and wave-averaged orbital motions and therefore do not resolve intra-wave  
621 transport mechanisms. Furthermore, the use of the parameter settings in  
622 Table 1 with the Kingsday version of XBeach allows bedload transport to be  
623 only onshore-directed, which is an unusual result that is repaired in subse-  
624 quent model releases. Nonetheless, an appropriate balance between onshore  
625 and offshore transport fluxes are obtained for our simulations despite these  
626 shortcomings. Further development of XBeach is therefore necessary to bet-  
627 ter and more realistically account for intra-wave and swash sediment trans-  
628 port processes. One suggestion to the model developers may be, for exam-  
629 ple, introducing acceleration dependent onshore fluxes as can be determined  
630 from gradients in the surface elevation computed by the non-hydrostatic wave  
631 solver.

## 632 **5. Conclusion**

633 A number of exploratory morphodynamic simulations were carried out to  
634 study beach cusp formation, inspired by observations at Nha Trang Beach,

635 Vietnam. The simulations used time-constant and time-varying (measured)  
636 wave forcing conditions. In the former, the length scale of cusp formations  
637 were analysed as a function of the significant wave height, mean wave period,  
638 directional spreading and angle of incidence ( $H_s$ ,  $T_m$ ,  $\sigma$  and  $\theta$ , respectively).  
639 The resulting cusp length scales varied according to well-established norms  
640 –  $H_s$  modulates cusp height and cross-shore depth, while  $T_m$ ,  $\sigma$  and  $\theta$  af-  
641 fect long-shore length scales. Cusps appear to be most prominent for longer  
642 period waves ( $> 10$  s) with moderate wave heights ( $> 1.3$  m). Slightly in-  
643 creased  $\sigma$  and  $\theta$  enhances long-shore length scales, but tends to make cusps  
644 less prominent at values  $> 10^\circ$ . The model was able to produce asymmetric  
645 cusp patterns for obliquely incident waves.

646 Time-varying (measured) wave conditions with the native sediment size  
647 produced cusps with smaller length scales to those measured; however, it may  
648 be possible to achieve a more comparable spacing by including directional  
649 variations. Reducing the median sediment diameter,  $D_{50}$ , in other simu-  
650 lations with time-varying wave conditions allowed more dissipative beach  
651 profiles to form, resulting in net erosion of the beachface (as opposed to ac-  
652 cretion in the previous simulations). Cusps were able to form under mildly  
653 erosive conditions (using  $D_{50} = 0.3$  mm), though not as prominent as when  
654 formed under accretive conditions. Cusps were not able to form under more  
655 intense erosion (using  $D_{50} = 0.2$  mm). This finding is in keeping with the  
656 many observations of cusps being found on coarse sand beaches rather than  
657 fine sand beaches. The model also showed a general tendency for coarse sed-  
658 iment to be located on cusp horns near the water line, though the inverse  
659 pattern was seen at other elevations on the beach face.



660 Given that the model is able to reasonably simulate the formation of  
661 cusps of varying length scales and prominence, the process of cusp initiation  
662 can be studied in more detail in future work. Initial results show there is  
663 a significant correlation between the long-shore wave height and bed level  
664 anomalies, which may be produced by wave reflection patterns as suggested  
665 in Almar et al. (2018). It is currently unknown to what extent edge waves  
666 play a role in cusp formation; however, this study provides a basis for more  
667 rigorous investigation of this enigmatic topic using the XBeach model.

## 668 **Acknowledgements**

669 This research has received support from French grants through ANR  
670 (COASTVAR: ANR-14-ASTR-0019) and CG29 subvention. The authors  
671 would like to thank all the participants present in the Nha Trang field exper-  
672 iment for the help provided. CD acknowledges the Conseil Départemental  
673 du Finistère, LabexMer (ANR-10-LABX-19), and the Marie Curie Prestige  
674 Fellowship Program for providing financial support for his postdoctoral re-  
675 search at UBO. CD also acknowledges Jaap Nienhuis and NSF Award No.  
676 1810855 for support during his postdoctoral stay at Florida State University.  
677 The authors thank Giovanni Coco and two other anonymous reviewers for  
678 their detailed comments and feedback, which greatly helped to improve the  
679 quality of the manuscript.

## 680 **Author Contributions**

681 FF, RA and LPA designed and carried out the field campaign and in-situ  
682 data collection at Nha Trang beach. MJ produced the orthophoto beach

683 DEM from the drone measurements. CD designed and performed the model  
684 simulations, post-processed measured data, analysed the model results and  
685 produced the figures. The manuscript was written and revised by CD, with  
686 comments from other co-authors.

### 687 **Conflicts of Interest**

688 The authors declare no conflict of interest.

### 689 **References**

- 690 Almar, R., Coco, G., Bryan, K., Huntley, D., Short, A., Senechal, N., 2008.  
691 Video observations of beach cusp morphodynamics. *Marine Geology* 254,  
692 216–223.
- 693 Almar, R., Lerma, A.N., Castelle, B., Scott, T., 2018. On the influence  
694 of reflection over a rhythmic swash zone on surf zone dynamics. *Ocean*  
695 *Dynamics* 68, 899–909.
- 696 Almeida, L.P., Almar, R., Blenkinsopp, C., Senechal, N., Bergsma, E.,  
697 Floc’h, F., Caulet, C., Biauxque, M., Marchesiello, P., Grandjean, P., Am-  
698 mann, J., Benschila, R., Thuan, D.H., Gomes da Silva, P., Viet, N.T.,  
699 2020. Lidar observations of the swash zone of a low-tide terraced trop-  
700 ical beach under variable wave conditions: The nha trang (vietnam)  
701 coastvar experiment. *Journal of Marine Science and Engineering* 8, 302.  
702 doi:doi:10.3390/jmse8050302.
- 703 Antia, E., 1987. Preliminary field observations on beach cusp formation and

704 characteristics on tidally and morphodynamically distinct beaches on the  
705 nigerian coast. *Marine Geology* 78, 23–33.

706 Bakhtyar, R., Barry, D., Jeng, D., Li, L., Yeganeh-Bakhtiary, A., 2009. Mod-  
707 eling sediment transport in the swash zone: A review. *Ocean Engineering*  
708 36, 767–783.

709 de Bakker, A., Tissier, M., Ruessink, B., 2014. Shoreline dissipation of in-  
710 fragravity waves. *Continental Shelf Research* 72, 73–82.

711 Coco, G., Burnet, T., Werner, B., Elgar, S., 2003. Test of self-organization  
712 in beach cusp formation. *J. Geophys. Res* 108, 3101.

713 Coco, G., Huntley, D., O’Hare, T., 2000. Investigation of a self-organization  
714 model for beach cusp formation and development. *Journal of Coastal*  
715 *Research* 105, 21991–22002.

716 Coco, G., Huntley, D., O’Hare, T., 2001. Regularity and randomness in the  
717 formation of beach cusps. *Marine Geology* 178, 1–9.

718 Coco, G., O’Hare, T., Huntley, D., 1999. Beach cusps: a comparison of data  
719 and theories for their formation. *Journal of Coastal Research* 15, 741–749.

720 Daly, C., Floc’h, F., Almeida, L.P., Almar, R., 2017. Modelling accretion at  
721 nha trang beach, vietnam. *Proceedings of the International Conference on*  
722 *Coastal Dynamics, Helsingor, Denmark* , 1886–1896.

723 Dodd, N., Stoker, A., Calvete, D., Sriariyawat, A., 2008. On beach cusp  
724 formation. *Journal of Fluid Mechanics* 597, 145–169.

- 725 Dubois, R.N., 1981. Foreshore topography, tides, and beach cusps, delaware.  
726 Geological Society of America Bulletin 92, 132–138.
- 727 Elgar, S., Gallagher, E., Guza, R., 2001. Nearshore sandbar migration. Jour-  
728 nal of Geophysical Research 106, 11623–11627.
- 729 van Gaalen, J., Kruse, S., Coco, G., Collins, L., Doering, T., 2011. Observa-  
730 tions of beach cusp evolution at melbourne beach, florida, usa. Geomor-  
731 phology 129.
- 732 Garnier, R., Ortega-Sanchez, M., Losada, M., Falques, A., Dodd, N., 2010.  
733 Beach cusps and inner surf zone processes: growth or destruction? a  
734 case study of trafilgar beach (cadiz, spain). Scientia Marina 74, 539–553.  
735 doi:10.3989/scimar.2010.74n3539.
- 736 Guza, R., Inman, D., 1975. Edge waves and beach cusps. Journal of Geo-  
737 physical Research: Oceans and Atmosphere 80, 2997–3012.
- 738 Holland, K., 1998. Beach cusp formation and spacings at duck, usa. Conti-  
739 nental Shelf Research 18, 1081–1098.
- 740 Holland, K., Holman, R., 1996. Field observations of beach cusps and swash  
741 motions. Marine Geology 134, 77–93.
- 742 Inman, D., Guza, R., 1982. The origin of swash cusps on beaches. Marine  
743 Geology 49, 133–148.
- 744 Kaneko, A., 1985. Formation of beach cusps in a wave tank. Coastal Engi-  
745 neering 9, 81–98.

- 746 Lashley, C.H., Roelvink, D., van Dongeren, A., Buckley, M.L., Lowe, R.J.,  
747 2018. Nonhydrostatic and surfbeat model predictions of extreme wave  
748 run-up in fringing reef environments. *Coastal Engineering* 137, 11–27.
- 749 Masselink, G., Hegge, B.J., Pattiaratchi, C.B., 1997. Beach cusp morphody-  
750 namics. *Earth Surface Processes and Landforms* 22, 1139–1155.
- 751 Masselink, G., Pattiaratchi, C., 1998a. Morphodynamic impact of sea breeze  
752 activity on a beach with beach cusp morphology. *Journal of Coastal Re-  
753 search* 14, 393–406.
- 754 Masselink, G., Pattiaratchi, C., 1998b. Morphological evolution of beach  
755 cusps and associated swash circulation patterns. *Marine Geology* 146,  
756 93–113.
- 757 McCall, R., Masselink, G., Roelvink, J., Russell, P., Davidson, M., Poate, T.,  
758 2012. Modeling overwash and infiltration on gravel barriers. *Proceedings  
759 of the 33rd International Conference on Coastal Engineering, Santander,  
760 Spain* .
- 761 Nolan, T., Kirka, R., Shulmeister, J., 1999. Beach cusp morphology on sand  
762 and mixed sand and gravel beaches, south island, new zealand. *Marine  
763 Geology* 157, 185–198.
- 764 O’Dea, A., Brodie, K., 2019. Spectral analysis of beach cusp evolution using  
765 3d lidar scans. *Proceedings of the 9th International Conference on Coastal  
766 Sediments, Tampa/St. Petersburg, Florida, World Scientific* , 657–673.
- 767 Rasch, M., Nielsen, J., Nielsen, N., 1993. Variations of spacings between

768 beach cusps discussed in relation to edge wave theory. *Geografisk Tidsskrift*  
769 - *Danish Journal of Geography* 93, 49–55.

770 van Rhee, C., 2010. Sediment entrainment at high flow velocity. *Journal of*  
771 *Hydraulic Engineering* 136, 572–582.

772 van Rijn, L., 2007a. Unified view of sediment transport by currents and  
773 waves. i: initiation of motion, bed roughness, and bed-load transport.  
774 *Journal of Hydraulic Engineering* 133, 649–667.

775 van Rijn, L., 2007b. Unified view of sediment transport by currents and  
776 waves. ii: suspended transport. *Journal of Hydraulic Engineering* 133,  
777 668–689.

778 Roelvink, D., van Dongeren, A., McCall, R., Hoonhout, B., van Rooijen,  
779 A., van Geer, P., de Vet, L., Nederhoff, K., Quataert, E., 2015. Xbeach  
780 technical reference: Kingsday release model description and reference guide  
781 to functionalities. Deltares, UNESCO-IHE Institute of Water Education  
782 and Delft University of Technology .

783 Roelvink, D., van Dongeren, A., McCall, R., Hoonhout, B., van Rooijen,  
784 A., van Geer, P., de Vet, L., Nederhoff, K., Quataert, E., 2018. Im-  
785 proving predictions of swash dynamics in xbeach: The role of groupi-  
786 ness and incident-band runup. *Coastal Engineering* 134, 103–123.  
787 doi:doi.org/10.1016/j.coastaleng.2017.07.004.

788 Roelvink, D., Reniers, A., van Dongeren, A., van Thiel de Vries, J., McCall,  
789 R., Lescinski, J., 2009. Modelling storm impacts on beaches, dunes and  
790 barrier islands. *Coastal Engineering* 56, 1133–1152.

- 791 Ruessink, B., Ramaekers, G., van Rijn, L., 2012. On the parameterization  
792 of the free-stream non-linear wave orbital motion in nearshore morphody-  
793 namic models. *Coastal Engineering* 65, 56–63.
- 794 Ruffini, G., Briganti, R., Alsina, J.M., Brocchini, M., 2020. Nu-  
795 merical modeling of flow and bed evolution of bichromatic wave  
796 groups on an intermediate beach using nonhydrostatic xbeach. *Journal of Waterway, Port, Coastal, and Ocean Engineering* 146.  
797 doi:doi.org/10.1061/(ASCE)WW.1943-5460.0000530.  
798
- 799 Sallenger, A., 1979. Beach cusp formation. *Marine Geology* 29, 23–37.
- 800 Soulsby, R., 1997. *Dynamics of marine sands: a manual for practical appli-*  
801 *cations.* Thomas Telford Publications, London.
- 802 Sunamura, T., 2004. A predictive relationship for the spacing of beach cusps  
803 in nature. *Coastal Engineering* 51, 697–711.
- 804 Talmon, A., van Mierlo, M., Struiksmā, N., 1995. Laboratory measurements  
805 of the direction of sediment transport on transverse alluvial-bed slopes.  
806 *Journal of Hydraulic Research* 33, 495–517.
- 807 Voudoukas, M., 2012. Erosion/accretion patterns and multiple beach cusp  
808 systems on a meso-tidal steeply-sloping beach. *Geomorphology* 141-142,  
809 34–46.
- 810 Walstra, D., van Rijn, L., van Ormondt, M., Briere, C., Talmon, A.M.,  
811 2007. The effects of bed slope and wave skewness on sediment transport  
812 and morphology. *Proceedings of the Sixth International Symposium on*  
813 *Coastal Sediments, ASCE* , 137–150.

- 814 van der Werf, J., Ribberink, J., Kranenburg, W., Neessen, K., Boers, M.,  
815 2017. Contributions to the wave-mean momentum balance in the surf  
816 zone. *Coastal Engineering* 121, 212–220.
- 817 Werner, B., Fink, T., 1993. Beach cusps as self-organized patterns. *Science*  
818 260, 968–971.
- 819 Zijlema, M., Stelling, G.S., Smit, P.B., 2011. Swash: An operational public  
820 domain code for simulating wave fields and rapidly varied flows in coastal  
821 waters. *Coastal Engineering* 58, 992–1012.